

Article pubs.acs.org/acsapm

Through-Thickness Modulus Gradient and Pattern Fidelity of UV-**Cured Thiol-Acrylate Films**

Amir Darabi and Lewis M. Cox*



Cite This: ACS Appl. Polym. Mater. 2024, 6, 9512-9520



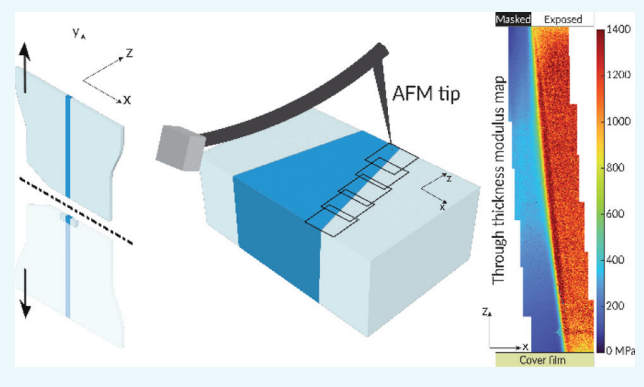
ACCESS I

III Metrics & More

Article Recommendations

Supporting Information

ABSTRACT: The utilization of photopolymers in diverse applications such as microfluidic devices, gas inhibitors, and biomimetic tissues has surged due to advancements in digital light processing technologies that now support multimaterial platforms, facilitating micrometer-scale control over material heterogeneity. However, significant knowledge gaps remain in our understanding of spatiotemporal evolution within these multimaterial actinic films and layers. To help bridge these gaps, a thiol-acrylate system is employed for photopatterning, and atomic force microscopy is leveraged to map through-thickness modulus profiles at various UV exposure levels, in both flood and masked curing setups. This approach enables the evolution of material properties to be tracked through the film thickness for incremental light exposure durations



and across different photopatterned feature sizes. The results illustrate complicated modulus profiles that highlight the complex interplay among light exposure parameters, polymerization kinetics, oxygen inhibition, and light scattering.

KEYWORDS: photopolymerization, thiol-acrylate, pattern fidelity, modulus gradients, oxygen inhibition

1. INTRODUCTION

Photopolymers are increasingly utilized across diverse applications, including the fabrication of microfluidic devices, gas inhibitors, and biomimetic tissues. 1-4 This surge in usage can be attributed to a shift in digital light processing (DLP) technologies from single-material printing paradigms to the emergent multimaterial platforms that provide micrometer and potentially submicron control over heterogeneity. 5-9 DLP processes photopolymers by building objects layer by layer, enabling the manipulation of mechanical properties through controlled light exposure. 3,10 An ongoing challenge in layer-bylayer printing is the uncertainty over material properties through the thickness of a single printed layer. Despite the expansive literature on the kinetics of photopolymerization, 11-14 significant gaps remain in our understanding of spatiotemporal evolution within heterogeneous photopatterned layers.

Local material characteristics in photopolymer systems are influenced by the degree of polymerization. In network forming resins, progressing monomer conversion is associated with higher cross-link densities and increasing elastic modulus. $^{15-20}$ If the mechanical properties of a cured actinic resin are a function of the total energy dose (the product of intensity and duration) only, then the system is considered reciprocal, and material properties, along with degree and depth of curing, are readily predictable. ^{21,22} This phenomenon is captured in "working curve" models, which predict cure

depth based on light exposure parameters.^{23–26} In general, these models predict that the cross-link density in a lightexposed region diminishes over the thickness of polymer films, yielding inferior mechanical properties toward the far end.

However, there are practical limitations to reciprocity law, and covariates, such as oxygen inhibition, photobleaching, and heat generation, undermine its predictions. 21,27-29 Additionally, in single-film processing applications, use of a photomask can impart additional complexities in material heterogeneity.³⁰ A thorough investigation into the through-thickness modulus variations in photopolymer films remains outstanding, and such studies are crucial for controlling material heterogeneity on different scales.

This research focuses on a thiol-acrylate photopolymer system, exploring the orthogonal reactions that drive its polymerization. An initial Michael addition click reaction provides a rubbery network,³¹ and subsequent radicalmediated acrylate homopolymerization is characterized via atomic force microscopy (AFM) through the film thickness. AFM modulus maps are collected at several UV exposure

Received: April 24, 2024 Revised: June 28, 2024 Accepted: August 7, 2024 Published: August 13, 2024





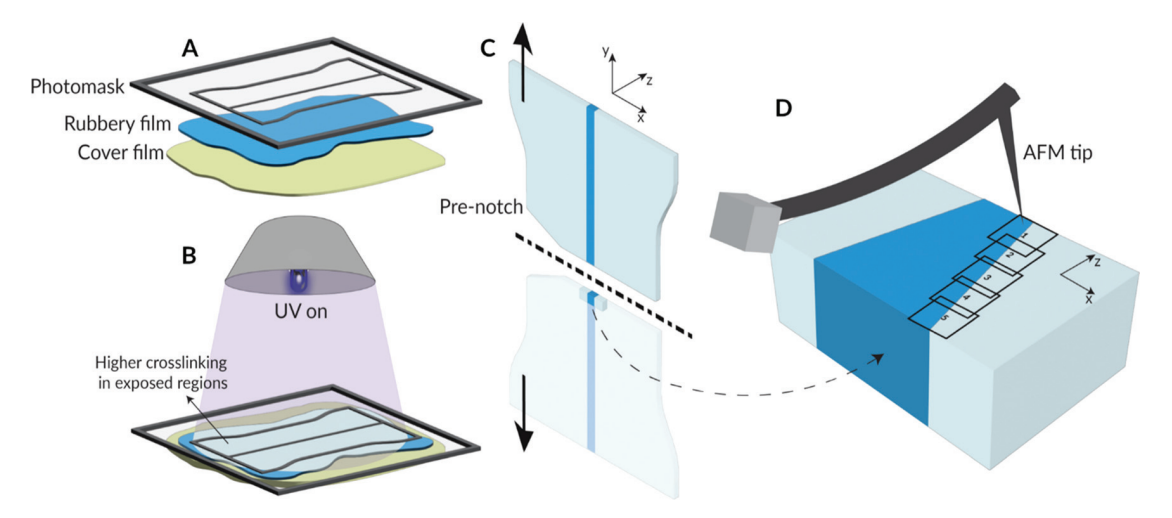


Figure 1. (A) Schematic of the UV-curing setup, where the rubbery film is laminated between the superstrate photomask (top) and the substrate cover film (bottom). (B) Rubbery film begins the transition to a glassy state upon UV exposure. (C) Prenotched photopatterned film is fractured along the patterned line to achieve a smooth cross section. (D) Film's cross section is scanned using AFM with several overlapping scans for subsequent stitching to achieve a through-thickness modulus map.

durations to spatially resolve network evolution from a rubbery state through the leathery transition regime and into a glassy state. Both flood and masked curing setups are employed, and consideration is given to the length scale of the masked features. The insights gained here will further our ability to precisely engineer the mechanical behavior of photopolymers in technologically relevant applications.

2. MATERIALS AND METHODS

2.1. Materials. Pentaerythritol tetrakis(3-mercaptopropionate) (PETMP), trimethylolpropane triacrylate (TMPTA), 2,2-Dimethoxy-2-phenylacetophenone (DMPA), triethylamine (TEA), and butylated hydroxytoluene (BHT) were procured from Sigma-Aldrich. The chemical structures of chemicals are shown in Figure S1 in the Supporting Information.

2.2. Film Processing. An off-stoichiometric ratio of 1:2.75 is selected between the thiol (PETMP) and acrylate (TMPTA) functional groups with excess acrylates. TEA (0.1 wt %) is added as the catalyst, and DMPA (1.5 wt %) is added as the photoinitiator. A trace amount of BHT (0.05 wt %) is added as the inhibitor to improve the shelf life of the polymer. All chemicals were purchased from Sigma-Aldrich. The first polymerization process, initiated upon the mixture, is a step-growth Michael addition "click" reaction between thiol and acrylate monomers. The solution is cast on large glass slides $(4 \times 5'')$ and allowed to reach full conversion overnight. To ensure uniform thickness, shim stock sheets of known thickness are placed on the glass slides as spacers (see Figure S1 in the Supporting Information). The result is a rubbery polymer film with excess unreacted acrylate functional groups and an average thickness of 100 \pm 6 μ m across all synthesized polymer films. Therefore, slight variations in film thickness are neglected in this work.

The "top" surface of the rubbery film is then laminated by hand against a soda lime superstrate photomask with etched-chrome patterns. This is accomplished by bringing one edge of the sample surface into contact with the photomask and then allowing that contact region to spread outward as the sample is gently "rolled" onto the mask. A visual inspection is then performed to ensure no obvious air bubbles have been trapped between the mask and sample. The treatment of the bottom surface in this work is noteworthy. To mitigate light reflection back into samples, index-matching oils and neutral density filters are commonly applied along the "bottom" of samples in curing setups. However, these oils were observed to contaminate the sample surfaces and frustrate AFM characterization. To preserve the cleanliness of surfaces, an index-matching rubbery

cover film is made from a 1:1 stoichiometric ratio of PETMP and TMPTA and rolled against the bottom surface using the previously described lamination technique. For context, an additional benefit of using index-matching oils and neutral density filters is the mitigation of oxygen inhibition during the curing process. The diffusivity of oxygen in the present material system is not explicitly measured but can be approximated from other thiol-ene rubbers in the literature (see Section S3 in the Supporting Information). While orders of magnitude lower than PDMS (commonly used in DLP processes), the diffusivity of oxygen through the index-matching cover film used as a substrate in this study is much higher than that of the soda lime photomask and traditional neutral density filters. Accordingly, the substrate may act as a limited reservoir for the diffusion of molecular oxygen into the sample during curing. The potential impacts of this boundary condition are discussed in Section 3.1. The configuration of the described material stack is depicted in Figure 1A. The stack is then positioned above a black felt box prior to illumination.

Upon exposure to ultraviolet (UV) light (OmniCure S1500 lamp, $300-400\,$ nm wavelength filter, $30\,$ mW/cm²), the photoinitiator generates free radicals that initiate the homopolymerization of excess acrylates in the polymer network, increasing the cross-linking density and elastic modulus in illuminated regions, Figure 1B. ³² UV exposure time is set to 0.5, 1, 3, 10, 30, and 300 s, translating to energy doses of 15, 30, 90, 300, 900, and 9000 mJ/cm², respectively. Four different feature widths of 10, 20, 50, and 100 μ m are photopatterned on polymer films. The UV light is subsequently absorbed by a box filled with black felt (see Figure S1 in the Supporting Information).

2.3. Tensile Testing. Polymer films are patterned with three different interlayer geometries, consisting of one flat line and two sinusoidal geometries with amplitudes of 2 and 5 mm and a constant wavelength of 1.4 mm. Each geometry is patterned at four different interlayer widths of 10, 20, 50, and 100 μ m. The composite films have a dog-bone outline with a 15 mm length, a 9 mm width at the ends, and a 7 mm width at the middle of the specimens. Photopatterned films are subject to 2% strain ramp using dynamic mechanical analysis (DMA, Q800, TA Instruments) to measure the modulus of photopatterned composites across different line widths and patterns, with five replicates per group.

2.4. Atomic Force Microscopy. To obtain sufficiently flat cross sections, a pre notch was placed on the edge of the dog-bone samples (Figure 1C), which were subsequently stretched until failure. The fractured samples were taped to a 90° sample mount for imaging. Prior to modulus mapping, optical microscopy, followed by topographic tapping mode scans, was used to identify regions of the fracture surface that were both flat and oriented orthogonally to the

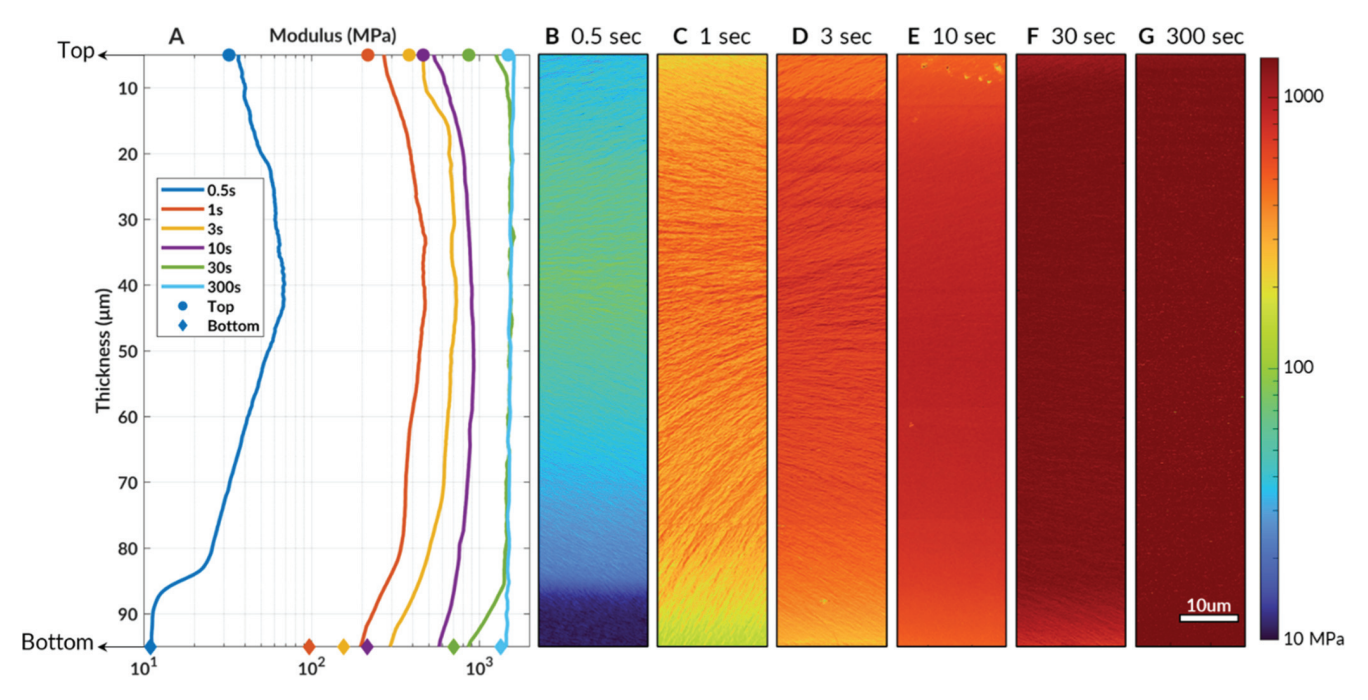


Figure 2. Through-thickness modulus gradient of flood-cured polymer films represented as (A) log-scale mean modulus, along with mean modulus of top and bottom surfaces, and (B–G) log-scale AFM color maps for 0.5–300 s UV exposures. The presented data illustrates the 5–95 μ m depth of the film cross section considering the challenges associated with scanning cross-sectional edges.

surfaces of the dog bone. A surface roughness on the order of 10s of nm is still observed on these samples of these surfaces. This roughness contains features of similar length scale to the probe tip and introduces a faint artifact into the modulus maps, as described in the discussion.

The fractured films are carefully mounted onto a metallic stage, orienting the cross section upward, for subsequent characterization using an atomic force microscope (AFM, Asylum Research Cypher S). Modulus maps are obtained through AFM fast force mapping mode using a 300 Hz scanning rate and a 40 N/m tip (Tap300Al-G, BudgetSensors). As shown in Figure 1D, multiple modulus maps are scanned with a small overlap to compile a comprehensive map of modulus variations throughout the thickness of the polymer films.

Fast force mapping is ideally suited for comparing the modulus values within a single scan. However, given that the objective of this study is to integrate multiple AFM maps, it becomes crucial to address potential inconsistencies arising from factors such as tip wear and tip contamination. To surmount this challenge, all maps associated with a single specimen are collected on the same day without removing the tip cantilever, using a consistent indentation force across multiple scans. An indentation force of 500 nN was selected due to its suitability for measuring both rubbery and glassy surfaces. This set point provides a good signal-to-noise ratio, and small changes to this value (±50 nN) do not result in significant changes to the measured modulus values of the sample. Calibration scans are conducted on the surface of a fully cured polymer film with a similar formulation to track any potential tip wear that rarely occurs after multiple scans.

2.5. Processing of Modulus Maps. To stitch modulus maps acquired from the film's cross section, we use a custom MATLAB code. This code combines raw data spreadsheets of overlapping AFM maps through the user identification of corresponding points. Stitched maps do not align in a perfectly linear fashion through the film thickness because (1) the work tracks certain interfacial features laterally, and (2) small amounts of lateral drift are generally unavoidable. The final, stitched data set is used to plot the throughthickness modulus map of the film. Some challenges that may question the reliability of modulus maps arise when regions are scanned close to the cross-sectional edges. These challenges are further discussed in Section 3.1.

3. RESULTS AND DISCUSSION

3.1. Evolution of Modulus Profiles during Flood Exposure. Rubbery films were flood-cured with UV at incremental exposure times, fractured to expose the cross section, and then imaged using AFM fast force mapping to quantify modulus variations through the thickness. Imaging the outermost edges of the cross-sectioned film presents two concerns: (1) the Hertzian contact model used to interpret force curves assumes an infinite substrate, and the presence of an edge impinging on the volume actuated by the AFM probe undermines this assumption in unknown ways; and (2) significant aggregations of dust and debris often occluded these regions of the surface (see Figure S2 in the Supporting Information). Accordingly, presented modulus maps exclude the upper and lower 5 μ m of the sample thickness, and modulus values at the edges are collected from the two film surfaces directly. During irradiation, the top side of every film was laminated against a transparent soda lime plate, and the bottom side was laminated against a cover film.

Figure 2A depicts the evolution of modulus gradients through the films' thickness, accompanied by the moduli measured at the top and bottom surfaces, for six incremental irradiation times of 0.5, 1, 3, 10, 30, and 300 s. Before discussing the evolution of the through-thickness modulus profiles, some observations should be noted. First, the horizontal lines in the modulus maps (especially evident in Figure 2D) are artifacts that occasionally appear during AFM scans. Second, the Hertzian contact mechanics model that is used to calculate the sample modulus from force-displacement data assumes the sample surface to be a flat plane. Surface topography and roughness have the potential to introduce artifacts into the modulus maps. In several stitched modulus maps, most strikingly evident in Figure 2C, a feathered texture is discernible as curved, linear features, submicrometer in width. It should be noted that these are

Table 1. Relative Standard Deviation for Each Modulus Profile

exposure duration (sec)	0.5	1	3	10	30	300
$RSD = \frac{\sigma_{E}}{\mu_{E}} \times 100\%$	33.67	19.71	19.22	12.83	9.42	2.62

 $^a\sigma_{\rm E}$ is the modulus standard deviation, and $\mu_{\rm E}$ is the modulus average.

artifacts that directly correspond to topographic features. Accordingly, the discussion that follows focuses on micrometer and larger-scale trends in the modulus gradients.

While the cross-sectional scans demonstrate that stiffness increases with exposure time, the modulus profiles contain interesting trends beyond this intuitive observation. For all tested exposure times of 30 s and less, the moduli near the top and bottom film surfaces are significantly lower than the moduli near the center of the films. The phenomenon is most pronounced at shorter exposure durations. After 0.5 s of exposure, a modulus of 30 MPa was measured at the top surface, increased until reaching a peak value of 70 MPa at a depth of approximately 45 μ m, decreased exponentially to 25 MPa at an approximate depth of 85 μ m thickness, and then sharply dropped to around 10 MPa and remained somewhat consistent for the 15 μ m adjacent to the bottom surface. Longer exposure times flatten out this profile, as shown in Table 1 comparing the relative standard deviation (RSD) of each modulus profile. While the 300 s sample shows excellent modulus uniformity, 30 s is enough to capture a relatively uniform glassy modulus throughout most of the film, with reductions in modulus observed only within $\sim 10 \mu m$ of the top surface and ~15 μ m of the bottom surface (RSD = 9.42%). This is a relevant consideration for time-sensitive layer-by-layer DLP applications.

To understand this data, light intensity as well as the concentration and diffusivity of oxygen and chemical species should be considered, but this endeavor is not trivial. As photopolymerization proceeds, the films evolve from a rubber, across their leathery glass transition regime, to a glass. Throughout this process, coefficients of diffusivity will change by an order of magnitude or more, and the concentrations of oxygen, photoinitiator, and free radicals will experience spatiotemporal complexity.

Specifically, upon UV exposure, DMPA breaks down and introduces free radicals in the network, leading to homopolymerization of excess acrylates and increasing cross-link density. While the specific relationship is complex and dependent on proximity to the material's glass transition regime, the modulus has a monotonic relationship with cross-linking density. At early exposure times, when DMPA concentration can be approximated as uniform, the light intensity will decrease as a function of depth, with an approximate 25% drop in intensity at the bottom of the 100 $\mu \rm m$ film, per Beer–Lambert law (see Figure S3 in the Supporting Information). The corresponding modulus profile would, in the absence of other covariates, monotonically decrease throughout the depth at early time periods in the curing process, but deviations from this trend are clear.

A likely covariate is oxygen, which inhibits free radical polymerization by scavenging radicals and forming peroxy radicals that cannot initiate polymerization immediately. 33,34 The diffusivity of oxygen $(D_{\rm O_2})$ in this material system is not known but can be approximated from measurements in similar materials (see Section S3 in the Supporting Information). $^{2,35-39}$ Employing a simple scaling relationship

$$\left(au=rac{L^2}{D_{\mathrm{O}_2}}
ight)$$
 to approximate the diffusion times (au) and length

(*L*) scales of oxygen indicates that the characteristic time scale for oxygen to diffuse across a 100 μm thick rubbery film falls in a range of 150 < $\tau_{\rm rubber}(\rm sec)$ < 200 in the initial rubbery film and increase to 2500 < $\tau_{\rm glass}(\rm sec)$ < 3800 in the fully cured, glassy network. At the shortest, 0.5 s exposure time, where the material is still predominantly rubbery, this corresponds to a characteristic diffusion length scale of ~5 μm , a value relevant to the observed length scales in the modulus profile associated with deviations from the monotonic trends expected from light absorption, warranting additional discussion.

Prior to UV exposure, polymer films are cast, covered in foil, and given 24 h for the initial step-growth polymerization to reach full conversion. Throughout the mixing, casting, and curing processes, oxygen is expected to diffuse into the samples. During the UV-curing process, oxygen can diffuse within the film, scavenging radicals, although the coefficient of diffusion of oxygen drops with increasing cross-link density. The potential for additional oxygen to enter the sample from the top and bottom surfaces is an important consideration. While imperfect sample lamination may trap small amounts of oxygen between the soda lime photomask, visual inspection was used to mitigate this chance, and diffusion across the soda lime plate itself is expected to be negligible across the time scales investigated here.

As mentioned earlier, the increasing modulus profile at the top half of the films, especially at shorter irradiation times of 0.5 and 1 s, is counterintuitive when compared to the light intensity profile. Although a simple explanation is not apparent, the authors infer that this phenomenon is caused by a competition between the light intensity and oxygen diffusion. The concentration of free radicals is highest at the incident surface due to the higher light intensity. The higher the concentration of free radicals, the larger the amounts of oxygen consumed, scavenging the free radicals near the top region. This could lead to an oxygen concentration gradient that causes the oxygen from within the film to diffuse upward to the top surface. However, this context is necessarily incomplete and requires investigations of spatiotemporal oxygen concentrations within the polymer in mask-based curing techniques.

The cover film at the bottom of the rubbery polymer is a soft material with diffusivity similar to that of the sample at short irradiation times and, thus, facilitates the diffusion of oxygen into the curing sample. This phenomenon, in addition to light attenuation, results in a relatively uniform 10 MPa "dead zone" anear the bottom of the film after 0.5 s of exposure in Figure 2A,B, where polymerization is almost entirely arrested. Although the modulus profile exhibits a minor gradient in this region, no measurable contrast in the modulus relative to the initial film stiffness is observed. Oxygen diffusivity within the network rapidly decreases with longer irradiations, and the stiffness within the dead zone increases measurably after 1 s of exposure. Even after curing begins, this region consistently exhibits the lowest modulus values for all irradiation times up until full conversion.

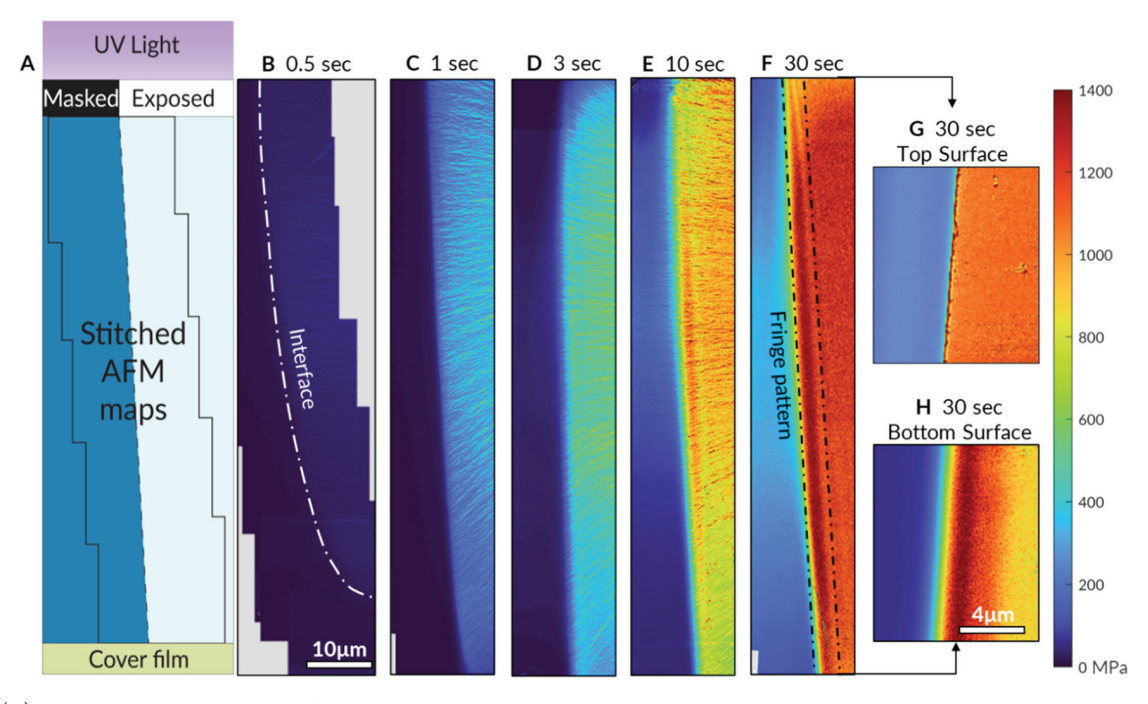


Figure 3. (A) Schematic of photopatterned film's cross section and overlapping AFM modulus maps that are stitched together. Masked areas in the superstrate photomask cover the film from incident light and inhibit immediate polymerization. (B-F) Through-thickness modulus map with exposure durations of 0.5-30 s. The interface does not extend throughout the film's cross section at 0.5 s exposure (B). Fringe patterns are formed at the masked/exposed boundary around the 1 s mark (C) and become more prominent at higher doses (D-F). (G) AFM scan from the top surface exhibits a sharp interface between masked and exposed regions, while (H) AFM scan from the bottom surface shows the irregularities at the interface due to the expansion of fringe pattern through the thickness.

Other covariates impacting modulus profiles include gradients in DMPA concentration as well as the moieties resulting from DMPA photolysis, known to cause minor variations in light absorption profiles over time. 44,45 While DMPA consumption is not tracked over time, the achievement of a uniform profile after 300 s indicates its residual presence, although it is still possible for polymerization to occur without the presence of photoinitiator at high doses. Finally, we note that thiol-ene systems have low susceptibility to UV degradation, and no evidence of degradation is observable in the modulus profile at 300 s UV exposure.

3.2. Evolution of Modulus Profiles during Photopatterning of a 10 μ m Line. Next, we employ a photomask pattern with a 10 μ m wide strip of chrome in a transparent field and characterize the evolution of a compliant line in a glassy matrix. A schematic of modulus mapping at the masked/ exposed interface, along with modulus profiles of photopatterned films with 0.5, 1, 3, 10, and 30 s exposure durations, is depicted in Figure 3. Upon illumination, an interface takes shape along the masked and exposed regions, Figure 3B. There are several consistencies between these results and those of the flood-cured samples. Specifically, the modulus is lower near the two surfaces and higher in the middle of the exposed region, with a similarly uncured region at the bottom of the film after 0.5 s of exposure, associated with an oxygen saturated region that inhibits cross-linking events. Eventually, a nearly uniform glassy profile, with drop-offs near the surfaces, is again reached after 30 s of exposure.

Below the masked feature's interface, an evolving modulus profile is observed through the thickness of the film. At early exposure times of 0.5 and 1 s, the boundary exhibits a parabolic shape, indicating that oxygen from the shaded material volumes is diffusing laterally into the exposed regions,

inhibiting polymerization. As oxygen inhibition is overcome at higher doses, this boundary evolves into a straight line, tilted around 2° off the vertical axis. Modulus maps of the top and bottom film surfaces indicate that the pattern in material modulus exhibits a 10 μ m line width on the top surface, consistent with the photomask geometry, and broadens to a thickness of approximately 12 μ m at the bottom surface. This feature broadening phenomenon may be attributed to the light scattering and flaring angle of light rays after colliding with the superstrate soda lime glass.

Another consistent phenomenon that appears at 1 s exposure and becomes more prominent with longer irradiations is the irregular fringe pattern in the modulus profile at the interface between the masked and exposed regions (Figure 3D-H). Light diffraction at the edge of the chrome mask and a resulting spatial pattern in light intensity is inferred to be the cause of the local modulus gradients at the interface. 48-50 This hypothesis is supported by the presence of a sharp interface in AFM modulus maps of the top surface (Figure 3G), which develops into a nonuniform interfacial modulus gradient that broadens as a function of depth through the film, evident on the bottom surface (Figure 3H). It is noteworthy that certain samples contained the unintended presence of particulate contaminants that generated similar fringe patterns within the illuminated volume (see Figure S4 in the Supporting Information).

The stability of the modulus in the masked regions is critical to a broad range of photopatterning applications. Figure 3 provides clear evidence of curing in masked regions, with a peak modulus of ~300 MPa arising in the middle of the 10 μ m feature after 30 s exposure. The modulus profile in the masked region exhibits minima in proximity to the surfaces and maximums near the center of the film thickness, a similar trend

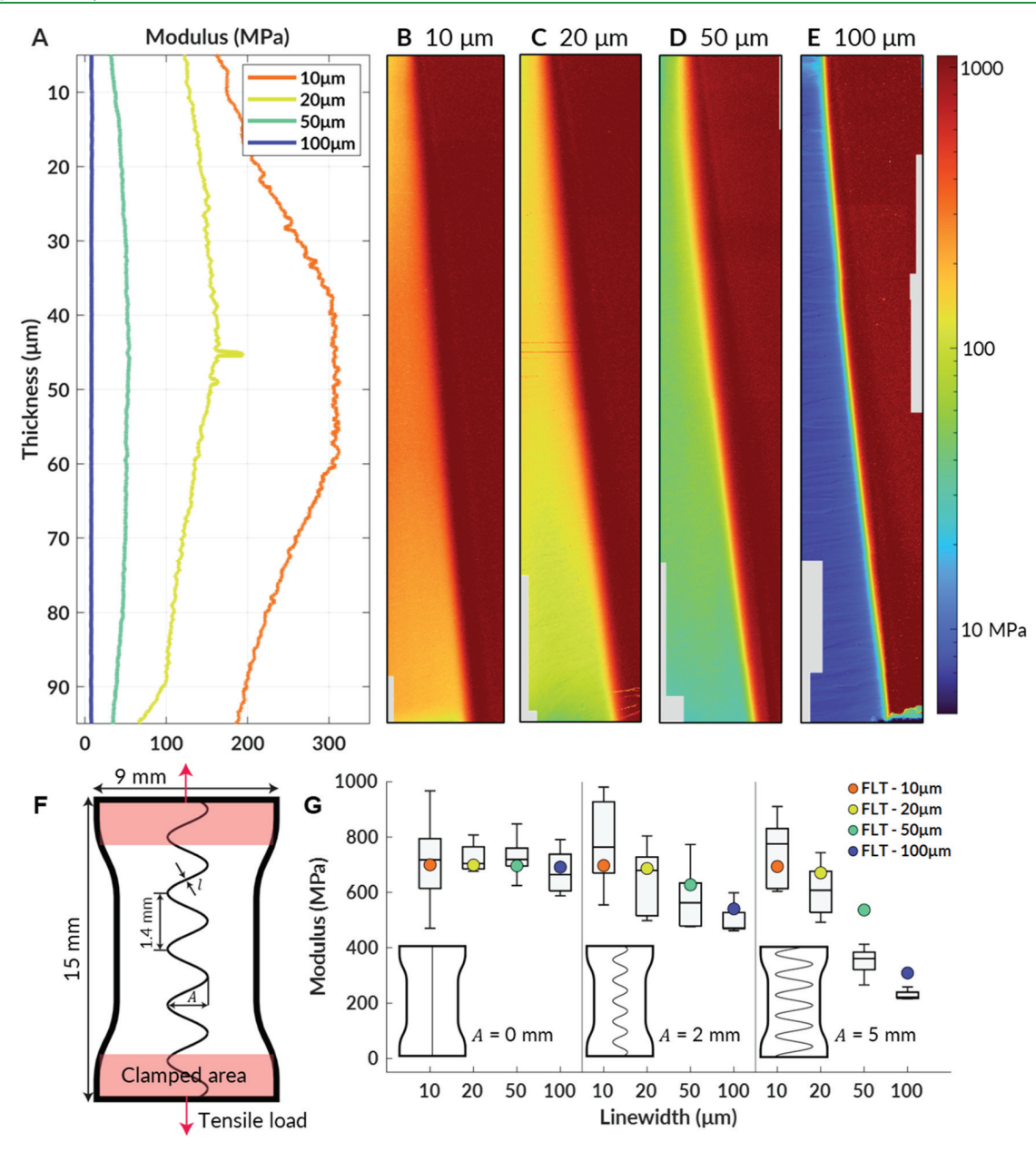


Figure 4. Through-thickness modulus gradient for four different feature sizes illustrated as (A) mean modulus of the masked region and (B-E) log-scale color maps. (F) Dog-bone sample outline and dimensions. Embedded sine waves have a wavelength of 1.4 mm, with the interlayer width (l) and amplitude (A) varying among different groups. It is worth noting that samples are not prenotched for tensile testing. (G) Modulus of composites embedded with various geometries reported by dynamic mechanical analysis, shown as box plots. Fiber laminate theory (FLT) is used to predict the composite modulus using data obtained from AFM, shown as dots.

observed in flood-cured films (Figure 2). Several factors such as light scattering and reflection, radical diffusion, and oxygen diffusion may contribute to the partial curing of the masked regions. Light reflection from the transparent substrate may contribute to the partial curing. Diffusion of free radicals from the exposed regions into the masked regions is possible at early time scales. However, unintended curing extends several micrometers into the masked region, and the characteristic diffusive length scales of radicals are likely significantly smaller than those of oxygen due to differences in the size of the diffusing molecules, so the effects are most likely relegated to submicrometer length scales adjacent to the interface. Still, additional investigations are needed to confirm this hypothesis.

3.3. Effect of the Line Width of Photopatterned Features on Through-Thickness Pattern Fidelity. In this section, we explore modulus profiles in the masked region for larger feature sizes of 20, 50, and 100 μ m and compare them to the 10 μ m line width. Here, an exposure duration of 30 s was selected since it results in near-uniformity and is comparable to exposure times and doses used in digital light processing techniques. ^{10,51,52}

For line widths of 10, 20, and 50 μ m, a nonuniform throughthickness profile is observed, with a maximum value near the center of the films (Figure 4B–D), consistent with flood curing results. The peak modulus of the masked feature scales inversely with the feature width. For a 10 μ m line width, modulus in the masked region increases to a maximum of 300

MPa in the middle (\sim 40–60 μ m) of the film thickness. This value drops to 160 and 60 MPa for line widths of 20 and 50 μ m, respectively. At the largest feature width of 100 μ m, the modulus is constant throughout the thickness and equal to the modulus of a rubbery film prior to UV exposure (\sim 10 MPa). These trends indicate that the final modulus of the masked regions is largely governed by competition of unintended dosing and oxygen inhibition. Larger feature sizes provide a larger reservoir of oxygen that will diffuse toward the maskedexposed interface and inhibit spurious polymerization. Smaller feature widths will result in a larger average dose within the masked volume and consume the oxygen dissolved in the masked regions of the network more rapidly. A scan of a 100 µm feature after 300 s of exposure (see Figure S4 in the Supporting Information) indicates that overexposure will eventually result in partial curing within these larger features, supporting the interpretation that oxygen inhibition is critical for the preservation of pattern fidelity.

3.4. Effect of Pattern Fidelity on Overall Mechanical Properties. Even if unintended curing is present, interrogating the degree to which it occurs enables better prediction of bulk composite properties for a given, arbitrary pattern. In a recent study, we examined the geometry–performance relationships of a wavy, compliant interlayer embedded within stiff matrices but were limited to larger, 100 μ m, interlayer widths due to unpredictable partial curing. Following the results displayed in Figure 4A–E, we apply fiber laminate theory (FLT) to anticipate the bulk modulus of composite films in relation to the interlayer's geometric features and compare FLT predictions with experimental data (see Section S5 in the Supporting Information).

Polymer films are photopatterned with three different amplitudes and four different interlayer widths for 30 s with a light intensity of 30 mW/cm². Specifications on interlayer geometries and sample dimensions are shown in Figure 4F. It is worth noting that the films embedded with flat line patterns are similar to the polymer films studied earlier. Box plots in Figure 4G show the modulus values obtained from dynamic mechanical analysis (DMA), with the upper and lower quartiles represented by the box and minimum and maximum values represented by the whiskers. The results indicate that the higher amplitudes exhibit lower moduli for an interlayer width of $100 \, \mu \text{m}$, but the contrast between different geometries diminishes with smaller feature sizes.

To estimate the overall modulus of the composite, FLT requires modulus values of the rubbery and glassy components. The bulk modulus of the glassy polymer is measured with DMA using flood-cured films and used in FLT. However, since measuring the bulk modulus of the partially cured interlayers is not possible, AFM modulus values exhibited in Figure 4A are averaged for each feature size and input in the FLT model (see Section S5 in the Supporting Information). FLT predictions of the composite modulus values are shown as circles in Figure 4G. Although discrepancies between macroscale and nanoscale modulus measurements are acknowledged, FLT results show an excellent ability to predict experimental measurements of bulk composite moduli associated with different interlayer line widths and waviness.

4. CONCLUSIONS

In this study, we investigated the evolution of modulus profiles in UV-cured, nonstoichiometric thiol-acrylate films, employing AFM fast force mapping to elucidate modulus variations through the films' thicknesses at various stages of UV exposure. Modulus profiles were examined in flood-cured films as well as films masked with a line feature of varying widths. Our findings provide new insights into the spatial variability of mechanical properties in these films, highlighting the influence of UV exposure time (and dose), oxygen diffusion, light diffraction, and light reflection on spatiotemporal modulus distributions.

Results revealed that while modulus generally increases with UV exposure time, nonuniform modulus gradients are readily observed through the thickness of films. Lower moduli are present near the top and bottom surfaces of a film's cross section, and peak modulus values are found near the center. This trend was especially pronounced at shorter exposure times, highlighting the complex interplay among light intensity profiles, oxygen diffusion, and polymerization kinetics. Observed modulus gradients diminish with longer exposure times, leading to a nearly uniform modulus profile after 30 s of exposure with gradients present only near the surfaces. A flat modulus profile is achieved through the thickness after 300 s.

Masked line features with widths of 10, 20, 50, and 100 μ m were photopatterned into films to create glassy composites with a compliant interlayer, and the fidelity of the compliant lines was characterized. Results show that smaller features exhibit greater degrees of unintended curing underneath the photomask, likely due to the reduced availability of oxygen reservoirs to inhibit curing coupled with increased light dosage. This was in contrast to larger features that exhibited excellent pattern fidelity and minimal spurious curing. The results from through-thickness modulus characterization were integrated into fiber laminate theory, demonstrating that a quantitative understanding of modulus drift in masked features enables the successful prediction of bulk composite properties for various interlayer geometries and line widths.

In conclusion, this study provides spatiotemporal characterization of modulus evolution in UV-photopatterned thiolacrylate films, offering insights that are critical for predicting and potentially optimizing photopolymerization processes and the mechanical properties of the resulting composites. Future work quantifying the evolution of oxygen and photoinitiator concentration gradients in these systems would address the limitations of this study and further refine our understanding of actinic polymerization processes.

ASSOCIATED CONTENT

Supporting Information

The Supporting Information is available free of charge at https://pubs.acs.org/doi/10.1021/acsapm.4c01257.

A schematic of UV-curing setup, AFM maps from crosssectional edges, light attenuation profile, estimation of oxygen diffusion coefficient, additional through-thickness modulus maps, and fiber laminate theory details (PDF)

AUTHOR INFORMATION

Corresponding Author

Lewis M. Cox — Department of Mechanical & Industrial Engineering, Montana State University, Bozeman, Montana 59717, United States; orcid.org/0000-0002-5830-3819; Email: lewis.cox@montana.edu

Author

Amir Darabi — Department of Mechanical & Industrial Engineering, Montana State University, Bozeman, Montana 59717, United States; Oorcid.org/0000-0001-7139-624X

Complete contact information is available at: https://pubs.acs.org/10.1021/acsapm.4c01257

Author Contributions

The manuscript was written through contributions of all authors. All authors have given approval to the final version of the manuscript. A.D: Conceptualization, methodology, formal Analysis, investigation, data curation, visualization, and writing—review and Editing L.M.C: Conceptualization, methodology, formal analysis, investigation, visualization, writing—review and editing, supervision, project administration, and funding acquisition.

Notes

The authors declare no competing financial interest.

ACKNOWLEDGMENTS

The authors thank Dr. Callie Higgins at the National Institute of Standards and Technology for providing insights on the collected data. The authors acknowledge funding support from the National Science Foundation under grant numbers CMMI-2038512 and CMMI-2038505. This work represents the views of the authors and not necessarily those of the sponsors.

REFERENCES

- (1) Paul, R.; Zhao, Y.; Coster, D.; Qin, X.; Islam, K.; Wu, Y.; Liu, Y. Rapid Prototyping of High-Resolution Large Format Microfluidic Device through Maskless Image Guided in-Situ Photopolymerization. *Nat. Commun.* **2023**, *14* (1), No. 4520, DOI: 10.1038/s41467-023-40119-x.
- (2) Blevins, A. K.; Cox, L. M.; Hu, L.; Drisko, J. A.; Lin, H.; Bowman, C. N.; Killgore, J. P.; Ding, Y. Spatially Controlled Permeability and Stiffness in Photopatterned Two-Stage Reactive Polymer Films for Enhanced CO2 Barrier and Mechanical Toughness. *Macromolecules* **2021**, *54* (1), 44–52.
- (3) Higgins, C. I.; Killgore, J. P.; DelRio, F. W.; Bryant, S. J.; McLeod, R. R. Photo-Tunable Hydrogel Mechanical Heterogeneity Informed by Predictive Transport Kinetics Model. *Soft Matter* **2020**, *16* (17), 4131–4141.
- (4) Levalley, P. J.; Noren, B.; Kharkar, P. M.; Kloxin, A. M.; Gatlin, J. C.; Oakey, J. S. Fabrication of Functional Biomaterial Microstructures by in Situ Photopolymerization and Photodegradation. *ACS Biomater Sci. Eng.* **2018**, *4* (8), 3078–3087.
- (5) Schwartz, J. J.; Boydston, A. J. Multimaterial Actinic Spatial Control 3D and 4D Printing. *Nat. Commun.* **2019**, *10* (1), No. 791, DOI: 10.1038/s41467-019-08639-7.
- (6) Rylski, A. K.; Maraliga, T.; Wu, Y.; Recker, E. A.; Arrowood, A. J.; Sanoja, G. E.; Page, Z. A. Digital Light Processing 3D Printing of Soft Semicrystalline Acrylates with Localized Shape Memory and Stiffness Control. ACS Appl. Mater. Interfaces 2023, 15 (28), 34097—34107.
- (7) Bagheri, A.; Jin, J. Photopolymerization in 3D Printing. ACS Appl. Polym. Mater. 2019, 1 (4), 593–611.
- (8) Limberg, D. K.; Kang, J. H.; Hayward, R. C. Triplet-Triplet Annihilation Photopolymerization for High-Resolution 3D Printing. *J. Am. Chem. Soc.* **2022**, *144* (12), 5226–5232.
- (9) Rylski, A. K.; Cater, H. L.; Mason, K. S.; Allen, M. J.; Arrowood, A. J.; Freeman, B. D.; Sanoja, G. E.; Page, Z. A. Polymeric Multimaterials by Photochemical Patterning of Crystallinity. *Science* **2022**, 378 (6616), 211–215.
- (10) Huh, J. T.; Moon, Y. W.; Park, J.; Atala, A.; Yoo, J. J.; Lee, S. J. Combinations of Photoinitiator and UV Absorber for Cell-Based

- Digital Light Processing (DLP) Bioprinting. *Biofabrication* **2021**, *13* (3). 034103.
- (11) Saenz-Dominguez, I.; Tena, I.; Sarrionandia, M.; Torre, J.; Aurrekoetxea, J. An Analytical Model of Through-Thickness Photopolymerisation of Composites: Ultraviolet Light Transmission and Curing Kinetics. *Composites, Part B* **2020**, *191*. 107963.
- (12) O'Brien, A. K.; Bowman, C. N. Modeling Thermal and Optical Effects on Photopolymerization Systems. *Macromolecules* **2003**, *36* (20), 7777–7782.
- (13) Camposeo, A.; Arkadii, A.; Romano, L.; D'Elia, F.; Fabbri, F.; Zussman, E.; Pisignano, D. Impact of Size Effects on Photopolymerization and Its Optical Monitoring In-Situ. *Addit. Manuf.* **2022**, *58*. 103020.
- (14) Courtecuisse, F.; Cerezo, J.; Croutxé-Barghorn, C.; Dietlin, C.; Allonas, X. Depth Characterization by Confocal Raman Microscopy of Oxygen Inhibition in Free Radical Photopolymerization of Acrylates: Contribution of the Thiol Chemistry. *J. Polym. Sci., Part A: Polym. Chem.*. **2013**, *51* (3), *635–643*.
- (15) Fiedler, C. I.; Aisenbrey, E. A.; Wahlquist, J. A.; Heveran, C. M.; Ferguson, V. L.; Bryant, S. J.; McLeod, R. R. Enhanced Mechanical Properties of Photo-Clickable Thiol-Ene PEG Hydrogels through Repeated Photopolymerization of in-Swollen Macromer. *Soft Matter* **2016**, *12* (44), 9095–9104.
- (16) Alketbi, A. S.; Shi, Y.; Li, H.; Raza, A.; Zhang, T. J. Impact of PEGDA Photopolymerization in Micro-Stereolithography on 3D Printed Hydrogel Structure and Swelling. *Soft Matter* **2021**, *17* (30), 7188–7195.
- (17) Peterson, G. I.; Schwartz, J. J.; Zhang, D.; Weiss, B. M.; Ganter, M. A.; Storti, D. W.; Boydston, A. J. Production of Materials with Spatially-Controlled Cross-Link Density via Vat Photopolymerization. *ACS Appl. Mater. Interfaces* **2016**, *8* (42), 29037–29043.
- (18) Chan, J. W.; Shin, J.; Hoyle, C. E.; Bowman, C. N.; Lowe, A. B. Synthesis, Thiol-Yne "Click" Photopolymerization, and Physical Properties of Networks Derived from Novel Multifunctional Alkynes. *Macromolecules* **2010**, *43* (11), 4937–4942.
- (19) Marklein, R. A.; Burdick, J. A. Spatially Controlled Hydrogel Mechanics to Modulate Stem Cell Interactions. *Soft Matter* **2010**, *6* (1), 136–143.
- (20) Fairbanks, B. D.; Scott, T. F.; Kloxin, C. J.; Anseth, K. S.; Bowman, C. N. Thiol-Yne Photopolymerizations: Novel Mechanism, Kinetics, and Step-Growth Formation of Highly Cross-Linked Networks. *Macromolecules* **2009**, *42* (1), 211–217.
- (21) Wydra, J. W.; Cramer, N. B.; Stansbury, J. W.; Bowman, C. N. The Reciprocity Law Concerning Light Dose Relationships Applied to BisGMA/TEGDMA Photopolymers: Theoretical Analysis and Experimental Characterization. *Dent. Mater.* **2014**, *30* (6), 605–612.
- (22) Mayerhöfer, T. G.; Mutschke, H.; Popp, J. Employing Theories Far beyond Their Limits—The Case of the (Boguer-) Beer-Lambert Law. *ChemPhysChem* **2016**, *17* (13), 1948–1955.
- (23) Jacobs, P. F. Rapid Prototyping & Manufacturing: Fundamentals of Stereolithography; Society of Manufacturing Engineers, 1992.
- (24) Uzcategui, A. C.; Muralidharan, A.; Ferguson, V. L.; Bryant, S. J.; McLeod, R. R. Understanding and Improving Mechanical Properties in 3D Printed Parts Using a Dual-Cure Acrylate-Based Resin for Stereolithography. *Adv. Eng. Mater.* **2018**, 20 (12), No. 1800876, DOI: 10.1002/adem.201800876.
- (25) Lee, J. H.; Prud'homme, R. K.; Aksay, I. A. Cure Depth in Photopolymerization: Experiments and Theory. *J. Mater. Res.* **2001**, *16* (12), 3536–3544.
- (26) Kolibaba, T. J.; Killgore, J. P.; Caplins, B. W.; Higgins, C. I.; Arp, U.; Miller, C. C.; Poster, D. L.; Zong, Y.; Broce, S.; Wang, T.; Talačka, V.; Andersson, J.; Davenport, A.; Panzer, M. A.; Tumbleston, J. R.; Gonzalez, J. M.; Huffstetler, J.; Lund, B. R.; Billerbeck, K.; Clay, A. M.; Fratarcangeli, M. R.; Qi, H. J.; Porcincula, D. H.; Bezek, L. B.; Kikuta, K.; Pearlson, M. N.; Walker, D. A.; Long, C. J.; Hasa, E.; Aguirre-Soto, A.; Celis-Guzman, A.; Backman, D. E.; Sridhar, R. L.; Cavicchi, K. A.; Viereckl, R. J.; Tong, E.; Hansen, C. J.; Shah, D. M.; Kinane, C.; Pena-Francesch, A.; Antonini, C.; Chaudhary, R.; Muraca, G.; Bensouda, Y.; Zhang, Y.; Zhao, X. Results of an Interlaboratory

- Study on the Working Curve in Vat Photopolymerization. *Addit. Manuf.* **2024**, *84*. 104082.
- (27) Miller, G. A.; Gou, L.; Narayanan, V.; Scranton, A. B. Modeling of Photobleaching for the Photoinitiation of Thick Polymerization Systems. *J. Polym. Sci., Part A: Polym. Chem.* **2002**, *40* (6), 793–808.
- (28) Rusu, M. C.; Block, C.; Van Assche, G.; Van Mele, B. Influence of Temperature and UV Intensity on Photo-Polymerization Reaction Studied by Photo-DSC. *J. Therm. Anal. Calorim.* **2012**, *110* (1), 287–294
- (29) Golaz, B.; Michaud, V.; Leterrier, Y.; Mnson, J. A. E. UV Intensity, Temperature and Dark-Curing Effects in Cationic Photo-Polymerization of a Cycloaliphatic Epoxy Resin. *Polymer* **2012**, *53* (10), 2038–2048.
- (30) Cox, L. M.; Blevins, A. K.; Drisko, J. A.; Qi, Y.; Ding, Y.; Fiedler, C. I.; Long, R.; Bowman, C. N.; Killgore, J. P.; Cox, L. M.; Killgore, J. P. Tunable Mechanical Anisotropy, Crack Guiding, and Toughness Enhancement in Two- Stage Reactive Polymer Networks. *Adv. Eng. Mater.* **2019**, *21* (8), No. 1900578, DOI: 10.1002/adem.201900578.
- (31) Nair, D. P.; Podgórski, M.; Chatani, S.; Gong, T.; Xi, W.; Fenoli, C. R.; Bowman, C. N. The Thiol-Michael Addition Click Reaction: A Powerful and Widely Used Tool in Materials Chemistry. *Chem. Mater.* **2014**, *26* (1), 724–744.
- (32) Nair, D. P.; Cramer, N. B.; McBride, M. K.; Gaipa, J. C.; Shandas, R.; Bowman, C. N. Enhanced Two-Stage Reactive Polymer Network Forming Systems. *Polymer* **2012**, *53* (12), 2429–2434.
- (33) O'Brien, A. K.; Cramer, N. B.; Bowman, C. N. Oxygen Inhibition in Thiol-Acrylate Photopolymerizations. *J. Polym. Sci., Part A: Polym. Chem.* **2006**, 44 (6), 2007–2014.
- (34) Cramer, N. B.; O'Brien, C. P.; Bowman, C. N. Mechanisms, Polymerization Rate Scaling, and Oxygen Inhibition with an Ultra-Rapid Monovinyl Urethane Acrylate. *Polymer* **2008**, 49 (22), 4756–4761.
- (35) Kwisnek, L.; Nazarenko, S.; Hoyle, C. E. Oxygen Transport Properties of Thiol-Ene Networks. *Macromolecules* **2009**, 42 (18), 7031–7041.
- (36) Kwisnek, L.; Kaushik, M.; Hoyle, C. E.; Nazarenko, S. Free Volume, Transport, and Physical Properties of n-Alkyl Derivatized Thiol-Ene Networks: Chain Length Effect. *Macromolecules* **2010**, 43 (8), 3859–3867.
- (37) Kwisnek, L.; Goetz, J.; Meyers, K. P.; Heinz, S. R.; Wiggins, J. S.; Nazarenko, S. PEG Containing Thiol-Ene Network Membranes for CO2 Separation: Effect of Cross-Linking on Thermal, Mechanical, and Gas Transport Properties. *Macromolecules* **2014**, 47 (10), 3243–3253.
- (38) Blevins, A. K.; Hu, L.; Azad, A. A.; Cox, L. M.; Killgore, J. P.; Lin, H.; Ding, Y. Impact of Interfaces on the CO2 Permeability of Photopatterned Two-Stage Thiolene Polymer Films. *Macromolecules* **2024**, *57* (3), 1354–1361.
- (39) Kwisnek, L.; Heinz, S.; Wiggins, J. S.; Nazarenko, S. Multifunctional Thiols as Additives in UV-Cured PEG-Diacrylate Membranes for CO2 Separation. *J. Membr. Sci.* **2011**, *369* (1–2), 429–436.
- (40) Asvany, O.; Yamada, K. M. T.; Brünken, S.; Potapov, A.; Schlemmer, S. Experimental Ground-State Combination Differences of CH5+. *Science* **2015**, 347 (6228), 1346–1348.
- (41) Taki, K. A Simplified 2D Numerical Simulation of Photopolymerization Kinetics and Oxygen Diffusion-Reaction for the Continuous Liquid Interface Production (CLIP) System. *Polymers* **2020**, *12* (4), 875.
- (42) Kim, D. S.; Suriboot, J.; Grunlan, M. A.; Tai, B. L. Feasibility Study of Silicone Stereolithography with an Optically Created Dead Zone. *Addit. Manuf.* **2019**, 29, No. 100793, DOI: 10.1016/j.addma.2019.100793.
- (43) Li, Y.; Mao, Q.; Yin, J.; Wang, Y.; Fu, J.; Huang, Y. Theoretical Prediction and Experimental Validation of the Digital Light Processing (DLP) Working Curve for Photocurable Materials. *Addit. Manuf.* 2021, 37, No. 101716.

- (44) Terrones, G.; Pearlstein, A. J. Effects of Optical Attenuation and Consumption of a Photobleaching Initiator on Local Initiation Rates in Photopolymerizations. *Macromolecules* **2001**, 34 (10), 3195–3204.
- (45) Mucci, V.; Vallo, C. Efficiency of 2,2-Dimethoxy-2-Phenylacetophenone for the Photopolymerization of Methacrylate Monomers in Thick Sections. *J. Appl. Polym. Sci.* **2012**, *123* (1), 418–425.
- (46) Cramer, N. B.; Reddy, S. K.; Cole, M.; Hoyle, C.; Bowman, C. N. Initiation and Kinetics of Thiol-Ene Photopolymerizations without Photoinitiators. *J. Polym. Sci., Part A: Polym. Chem.* **2004**, 42 (22), 5817–5826.
- (47) Hoyle, C. E.; Lee, T. Y.; Roper, T. Thiol-Enes: Chemistry of the Past with Promise for the Future. *J. Polym. Sci., Part A: Polym. Chem.* **2004**, 42 (21), 5301–5338.
- (48) Kumar, R.; Kaura, S. K.; Sharma, A. K.; Chhachhia, D. P.; Aggarwal, A. K. Knife-Edge Diffraction Pattern as an Interference Phenomenon: An Experimental Reality. *Opt. Laser Technol.* **2007**, 39 (2), 256–261.
- (49) Santhanakrishnan, T.; Rajesh, R.; Awasthi, R. L.; Sreehari, C. V. Optical Diffraction Phenomena around the Edges of Photodetectors: A Simplified Method for Metrological Applications. *Sci. Rep* **2019**, 9 (1), No. 3397, DOI: 10.1038/s41598-019-40270-w.
- (50) Cheng, Y.; Lin, C. Y.; Wei, D. H.; Loechel, B.; Gruetzner, G. Wall Profile of Thick Photoresist Generated via Contact Printing. *J. Microelectromech. Syst.* **1999**, 8 (1), 18–26.
- (51) Wu, D.; Zhao, Z.; Zhang, Q.; Qi, H. J.; Fang, D. Mechanics of Shape Distortion of DLP 3D Printed Structures during UV Post-Curing. Soft Matter 2019, 15 (30), 6151–6159.
- (52) Li, Y.; Mao, Q.; Li, X.; Yin, J.; Wang, Y.; Fu, J.; Huang, Y. High-Fidelity and High-Efficiency Additive Manufacturing Using Tunable Pre-Curing Digital Light Processing. *Addit. Manuf.* **2019**, 30, No. 100889.
- (53) Darabi, A.; Long, R.; Weber, J. C.; Cox, L. M. Effect of Geometry and Orientation on the Tensile Properties and Failure Mechanisms of Compliant Suture Joints. *ACS Appl. Mater. Interfaces* **2023**, *15* (8), 11084–11091.